Supporting Information for: "Hidden Hemibonding in the Aqueous Hydroxyl Radical"

Bhaskar Rana and John M. Herbert[*]

Department of Chemistry and Biochemistry
The Ohio State University, Columbus, Ohio 43210 USA

August 12, 2021

S1 Computational Details

All aiMD simulations were performed with CP2K,[1] using a $12.42 \times 12.42 \times 12.42$ Å^3 simulation cell containing $OH(H_2O)_{63}$, in order to avoid artifacts reported previously when the unit cell consists of $OH(H_2O)_{31}$.[2] These simulations employed the PBE0 + D3 density functional and the MOLOPT-DZVP-SR-GTH basis set along with the GTH-PBE pseudopotentials. A cutoff radius of 6.0 Å was used to truncate the interaction potential. An auxiliary density matrix scheme,[3] in which a smaller basis set is used to compute exact exchange, is employed to reduce the cost. The simulations employ a time step of 0.5 fs and a self-consistent field convergence threshold of 10^{-6} a.u., which is generally sufficient for energy conservation over picosecond trajectories.[4] The precision of the overlap matrix was set to 10^{-14} a.u. with a plane wave cutoff of 400 Ry and multigrid number 5, with a cutoff value of 40 Ry for mapping the Gaussians onto the grids. This computational setup is similar to what was reported in Ref. 5, which also examined $^\bullet$OH(aq) using hybrid functionals, except that the unit cell in Ref. 5 consisted of was $OH(H_2O)_{31}$ whereas the present cell is twice as large.

The aiMD simulations were initiated from an equilibrated classical MD simulation of neat liquid water obtained using the AMOEBA force field,[6] by removing one hydrogen atom near the center of the simulation cell. The DFT simulations were performed under constant NVT conditions using a Nosé-Hoover thermostat that was initially set to $T = 370$ K in order to make contact with simulations reported in Ref. 5. This trajectory was allowed to equilibrate for 10 ps and then production statistics were accumulated from a subsequent 15 ps of simulation time. A second trajectory at $T = 310$ K was initialized starting from the warmer trajectory and then equilibrated for 5 ps, followed by a 10 ps production run. Both temperatures are above the normal melting temperature of PBE0 + D3 water, which is $T = 268$ K.[7]

The electronic spectrum is computed as described in previous work.[8,9] Ensemble-averaged absorption spectra were computed using 600 snapshots extracted from the $T = 370$ K trajectory in 25 fs intervals. For each snapshot, a single-point QM/MM calculation was prepared in the following way. First, a $5 \times 5 \times 5$ supercell was constructed from the periodic unit cell, and from that supercell a QM region extending to a radius of 5.5 Å around the $^\bullet$OH radical was selected, containing 27–33 water molecules depending on the snapshot. The remaining atoms in the supercell were represented by MM point charges obtained from the simple point-charge (SPC) force field for water.[10] A TD-DFT QM/MM calculation was then performed within the Tamm-Dancoff approximation.[11] For calculations using the optimally-tuned[12] (OT) LRC-ωPBE functional,[13] the tuning procedure was carried out at 14 well-separated snapshots, affording an average range-separation parameter $\omega = 0.398$ a_0^{-1}. All TD-DFT calculations were performed using Q-Chem v. 5.3.[14]

MP2/6-31G* structure relaxations were performed using the resolution-of-identity (RI) approximation for the electron repulsion integrals, with the auxiliary basis developed for use with cc-pVDZ.[15]

---

[*]herbert@chemistry.ohio-state.edu

S2　References

[1] Kühne, T. D. *et al.* CP2K: An electronic structure and molecular dynamics software package—Quickstep: Efficient and accurate electronic structure calculations. *J. Chem. Phys.* **2020,** *152,* 194103.

[2] Codorniu-Hernández, E.;　Kusalik, P. G. Insights into the solvation and mobility of the hydroxyl radical in aqueous solution. *J. Chem. Theory Comput.* **2011,** *7,* 3725–3732.

[3] Guidon, M.;　Hutter, J.;　VandeVondele, J. Auxiliary density matrix methods for Hartree–Fock exchange calculations. *J. Chem. Theory Comput.* **2010,** *6,* 2348–2364.

[4] Herbert, J. M.;　Head-Gordon, M. Accelerated, energy-conserving Born-Oppenheimer molecular dynamics *via* Fock matrix extrapolation. *Phys. Chem. Chem. Phys.* **2005,** *7,* 3269–3275.

[5] Apostolidou, C. OH radical in water from *ab initio* molecular dynamics simulation employing hybrid functionals. *J. Chem. Phys.* **2019,** *151,* 064111.

[6] Ponder, J. W.;　Wu, C.;　Ren, P.;　Pande, V. S.;　Chodera, J. D.;　Schnieders, M. J.;　Haque, I.;　Mobley, D. L.;　Lambrecht, D. S.;　DiStasio, Jr., R. A.;　Head-Gordon, M.;　Clark, G. N. I.;　Johnson, M. E.;　Head-Gordon, T. Current status of the AMOEBA polarizable force field. *J. Phys. Chem. B* **2010,** *114,* 2549–2564.

[7] Reinhardt, A.;　Cheng, B. Quantum-mechanical exploration of the phase diagram of water. *Nat. Chem.* **2021,** *12,* 1–7.

[8] Uhlig, F.;　Herbert, J. M.;　Coons, M. P.;　Jungwirth, P. Optical spectroscopy of the bulk and interfacial hydrated electron from ab initio calculations. *J. Phys. Chem. A* **2014,** *118,* 7507–7515.

[9] Rana, B.;　Herbert, J. M. Role of hemibonding in the structure and ultraviolet spectroscopy of the aqueous hydroxyl radical. *Phys. Chem. Chem. Phys.* **2020,** *22,* 27829–27844.

[10] Berendsen, H. J. C.;　Postma, J. P. M.;　van Gunsteren, W. F.;　Hermans, J. Interaction models for water in relation to protein hydration. In *Intermolecular Forces*; Pullman, B.,　Ed.; Reidel: Dordrecht, Netherlands, 1981.

[11] Hirata, S.;　Head-Gordon, M. Time-dependent density functional theory within the Tamm-Dancoff approximation. *Chem. Phys. Lett.* **1999,** *314,* 291–299.

[12] Baer, R.;　Livshits, E.;　Salzner, U. Tuned range-separated hybrids in density functional theory. *Annu. Rev. Phys. Chem.* **2010,** *61,* 85–109.

[13] Rohrdanz, M. A.;　Martins, K. M.;　Herbert, J. M. A long-range-corrected density functional that performs well for both ground-state properties and time-dependent density functional theory excitation energies, including charge-transfer excited states. *J. Chem. Phys.* **2009,** *130,* 054112.

[14] Shao, Y. *et al.* Advances in molecular quantum chemistry contained in the Q-Chem 4 program package. *Mol. Phys.* **2015,** *113,* 184–215.

[15] Weigend, F.;　Köhn, A.;　Hättig, C. Efficient use of the correlation consistent basis sets in resolution of the identity MP2 calculations. *J. Chem. Phys.* **2002,** *116,* 3175–3183.

[16] Jacobson, L. D.;　Herbert, J. M. A one-electron model for the aqueous electron that includes many-body electron-water polarization: Bulk equilibrium structure, vertical electron binding energy, and optical absorption spectrum. *J. Chem. Phys.* **2010,** *133,* 154506.

[17] Czapski, G.;　Bielski, B. H. J. Absorption spectra of the $^\bullet$OH and O$^{\bullet-}$ radicals in aqueous solutions. *Radiat. Phys. Chem.* **1993,** *41,* 503–505.

[18] Chipman, D. M. Hemibonding between hydroxyl radical and water. *J. Phys. Chem. A* **2011,** *115,* 1161–1171.

[19] Baker, J.; Kessi, A.; Delley, B. The generation and use of delocalized internal coordinates in geometry optimization. *J. Chem. Phys.* **1996,** *105,* 192–212.

[20] Lange, A. W.; Herbert, J. M. A smooth, nonsingular, and faithful discretization scheme for polarizable continuum models: The switching/Gaussian approach. *J. Chem. Phys.* **2010,** *133,* 244111.

[21] Herbert, J. M. Dielectric continuum methods for quantum chemistry. *WIREs Comput. Mol. Sci.* **2021,** *11,* e1519.

S3 Additional Data
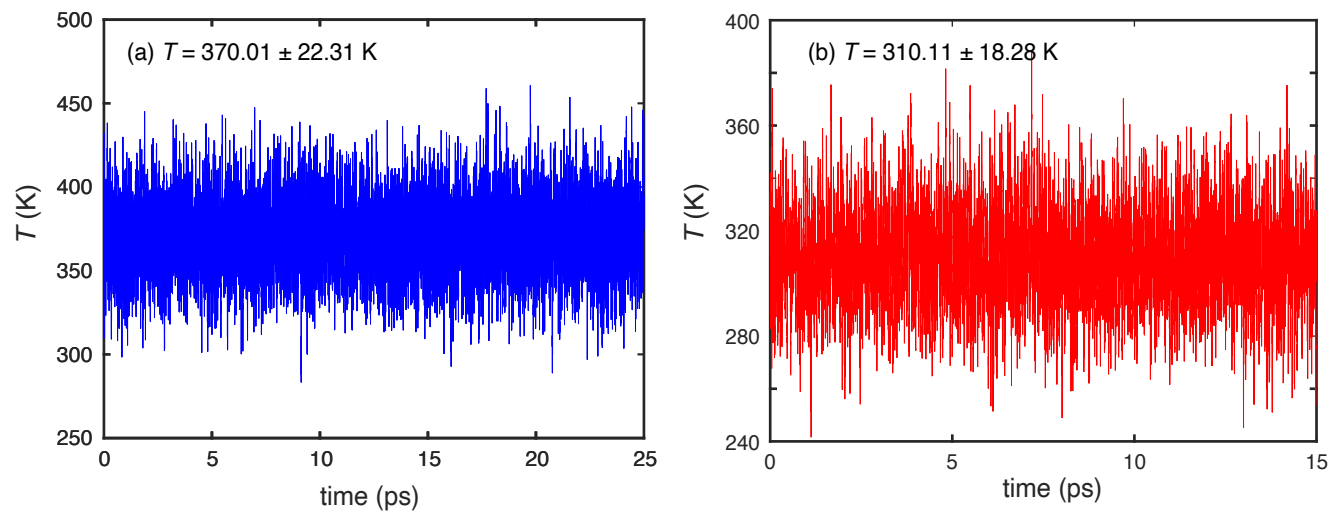
Figure S1: Time evolution of the instantaneous temperature for two NVT simulations of ${}^{\bullet}$OH(aq), at the PBE0 + D3 level. The average temperature and its standard deviation are indicated, from the production part of the simulation, meaning the final 15 ps in (a) and the final 10 ps in (b).
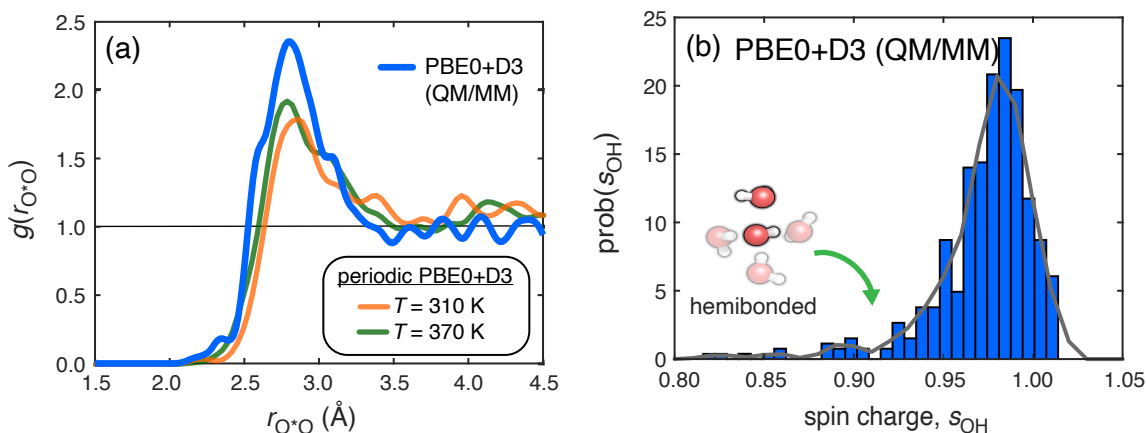
Figure S2: QM/MM results from a 5 ps trajectory (following 1 ps of equilibration) of a spherical water droplet containing 507 total water molecules, with an inner QM region consisting of $OH(H_2O)_{64}$ that is described at the PBE0 + D3/6-31G* level of theory. (a) RDFs $g(r_{O*O})$, comparing results from the periodic simulations (reproduced from Fig. 1b) to QM/MM result for the droplet, demonstrating reasonable qualitative agreement between these different simulation techniques. (b) Spin charge (s_{OH}) distribution for the droplet, which is a qualitative match to results from the the PBE0 + D3 periodic DFT trajectories in Fig. 2. Together, these comparisons indicate that the present QM/MM results are in reasonable agreement with the periodic DFT simulations, whereas the previous QM/MM simulations (from Ref. 9) are not, as can be seen in Fig. 1. The previous simulations used a large, periodic MM cell but a QM region consisting of only $OH(H_2O)_{31}$, whereas all simulations reported in the present work use a QM region that is twice as large. Discrepancies between $g(r_{O*O})$ reported in Ref. 9 and those reported herein are therefore attributable to finite-size effects on the QM region (despite the large surrounding MM region), rather than to any discrepancy between QM/MM versus periodic DFT.
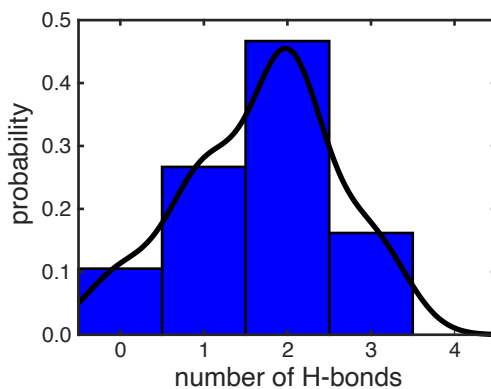
Figure S3: Histogram of the number of hydrogen bonds with $^{\bullet}OH$, calculated using the nearest five water molecules from the radical using the same angle-dependent distant cutoff as in previous work. [9,16] The histogram includes data from 600 snapshots, each separated by 25 fs in time.
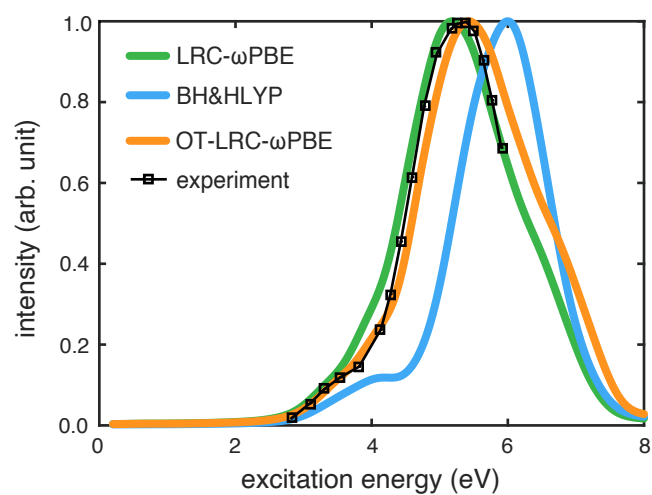
Figure S4: Comparison of TD-DFT absorption spectra in energy units. These are the same data that are plotted in wavelength units in Fig. 3a. The experimental data are from Ref. 17, corresponding to extinction coefficients measured via pulse radiolysis at 25°C. All spectra have been normalized to unit intensity at their respective maxima.
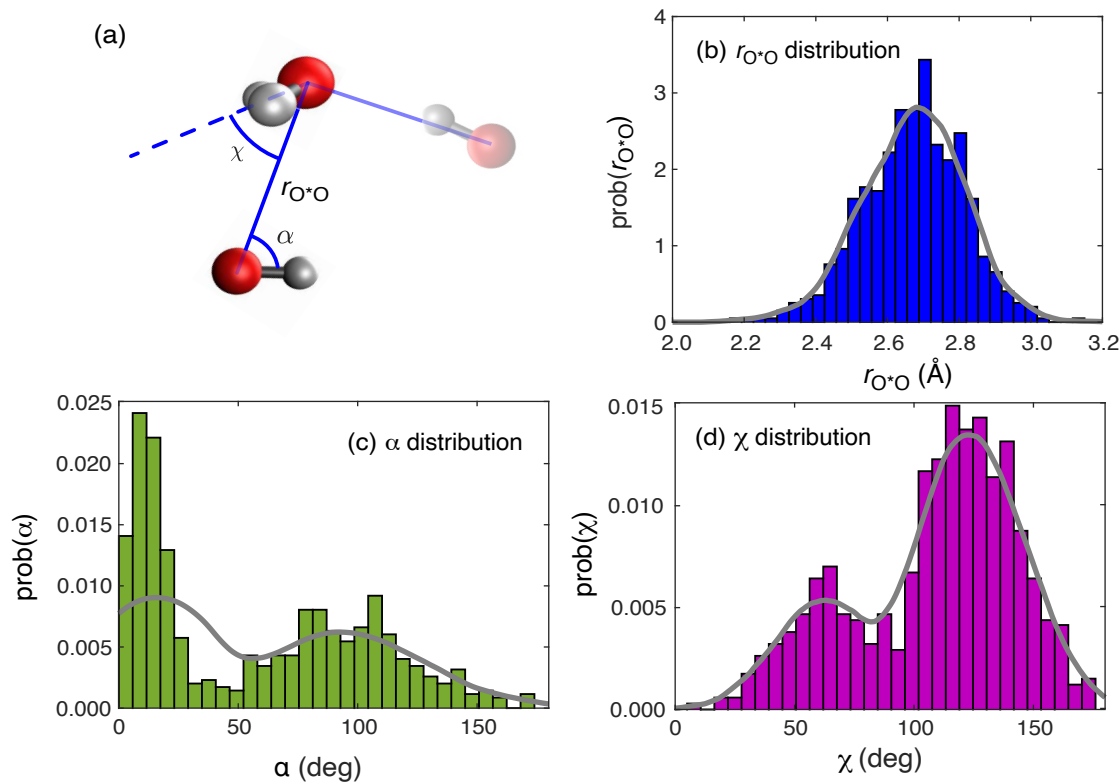
Figure S5: Probability distributions for the geometrical parameters r_{O^*O}, α, and χ that are indicated in panel (a), from the PBE0 + D3 trajectory at $T = 370$ K, Gray curves are fits to the distributions. As shown in Refs. 9 and 18, these parameters can be used to construct a geometric definition of the hemibond. All configurations (both hemibonded and non-hemibonded) are included in the histograms, and the bimodality of the angular distributions reflects that fact while the lack of bimodality in the r_{O^*O} distribution is a reflection of how the hemibonded $O^* \cdots O$ distance is hidden beneath a larger hydrogen-bonded distribution of $O^* \cdots O$ distances. All three distributions qualitatively match those obtained in QM/MM simulations using the LRC-ωPBE + D3 functional, in Ref. 9.
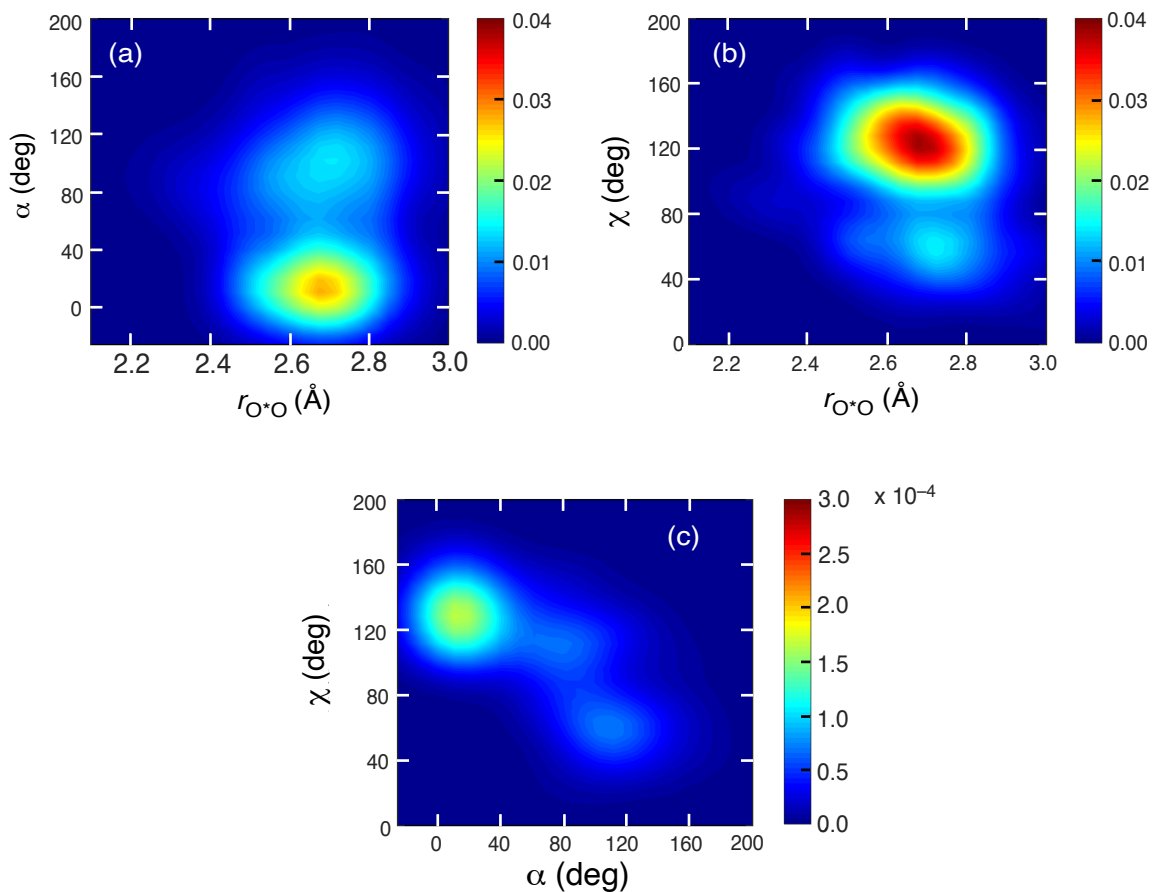
Figure S6: Joint probability distributions for the geometric parameters defined in Fig. S5a: (a) (r_{O^*O}, α) (b) (r_{O^*O}, χ) and (c) (α, χ). These are taken from the periodic PBE0+D3 trajectory at $T = 370$ K but all three joint distributions are similar to QM/MM results obtained using LRC-ωPBE+D3.[9] From these probability distributions emerges a similar geometry definition of hemibonded •OH as compared to the one put forward in Ref. 9, namely, $r_{O^*O} < 2.5$ Å, $70° \leq \alpha \leq 100°$, and also $70° \leq \chi \leq 100°$.
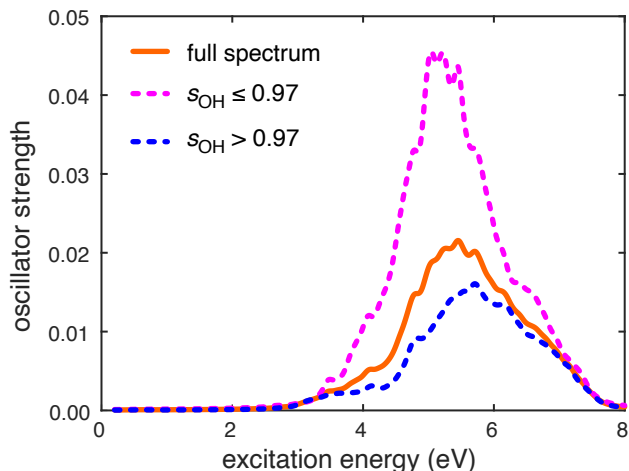
Figure S7: Comparison of the TD-DFT absorption spectra averaged over all the snapshots (black curve), versus decompositions that only include the hemibonded snapshots (orange curve) or the non-hemibonded snapshots (blue curve), as defined by the spin charge s_{OH}. This is the same partition as in Fig. 3b but what is plotted here is the total oscillator strength for each subset of snapshots. The hemibonded configurations contribute significantly more oscillator strength despite being outnumbered in a 1:3 ratio by the non-hemi-bonded configurations, because the most intense transition in each hemibonded configuration has an oscillator strength that is typically 4–5× larger than the most intense transition in a non-hemibonded configuration.
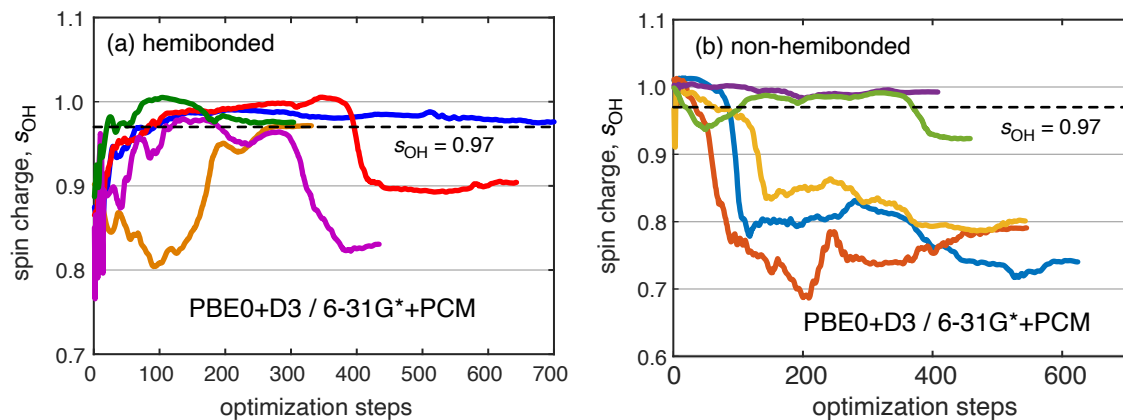
Figure S8: Geometry relaxations, via rational functional optimization in delocalized internal coordinates,[19] at the PBE0 + D3/6-31G* level of theory. The starting structures correspond to (a) hemibonded versus (b) non-hemibonded structures, extracted from a periodic PBE0 + D3 simulation by selecting all water molecules within 5.5 Å around the •OH radical. Geometry optimization was then performed using dielectric continuum boundary conditions, specifically, the conductor-like polarizable continuum model (C-PCM),[20] with a standard solvent-accessible cavity surface (Bondi radii and 1.4 Å probe radius for water).[21] Plotted here, along each optimization trajectory, is the spin charge s_{OH} on the radical, computed at the same level of theory that is used for the geometry optimization. The dashed line shows the value of s_{OH} that is used as a cutoff for the electronic definition of a hemibond.
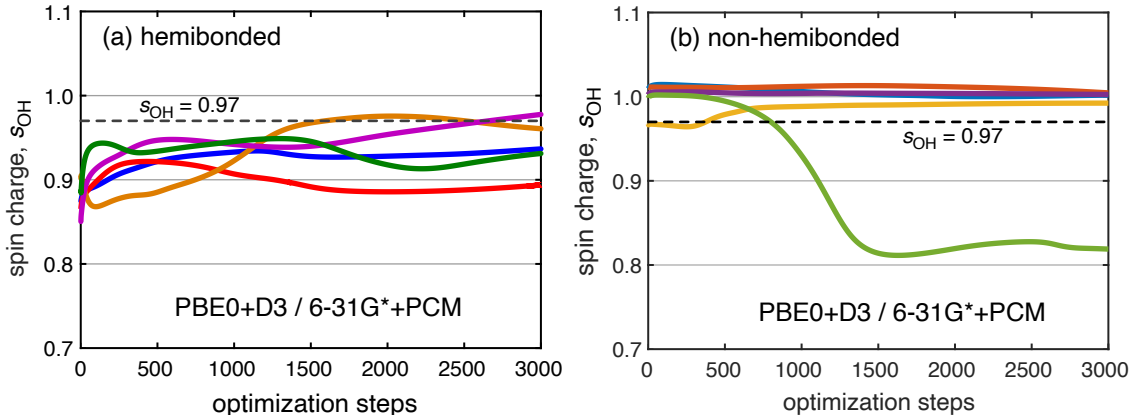
Figure S9: Geometry relaxations via steepest descent in Cartesian coordinates, at the PBE0 + D3/6-31G* level of theory. The setup is the same as that described in Fig. S8 and only the geometry optimization algorithm is changed. The steepest-descent algorithm, while highly inefficient, is more likely to find the local minimum that is closest to the starting structure without accidental basin-hopping into a different structure. The dashed line shows the value of s_{OH} that is used as a cutoff for the electronic definition of a hemibond.
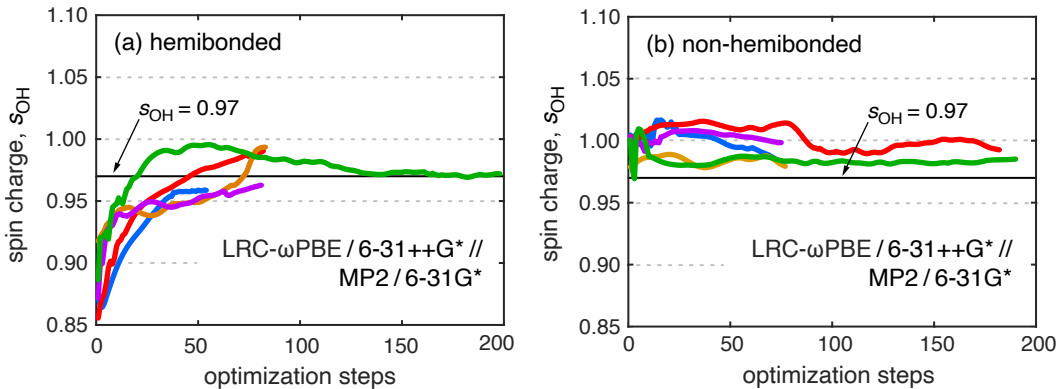
Figure S10: Geometry relaxations, using rational functional optimization in delocalized internal coordinates,[19] at the MP2/6-31G* level of theory. These calculations do not employ a continuum model. For comparison to DFT calculations presented elsewhere in this work, what is plotted here are the spin charges along the MP2 optimization trajectory, evaluated at the OT-LRC-ωPBE/6-31++G* level of theory. The horizontal black line indicates the value $s_{OH} = 0.97$ that is used as a cutoff for the electronic definition of a hemibond. Panel (a) shows initially hemibonded structures extracted from the periodic DFT simulations; these are the same data that are plotted in Fig. 5a. Panel (b) shows optimizations starting from structures that are *not* hemibonded in the periodic DFT simulations.
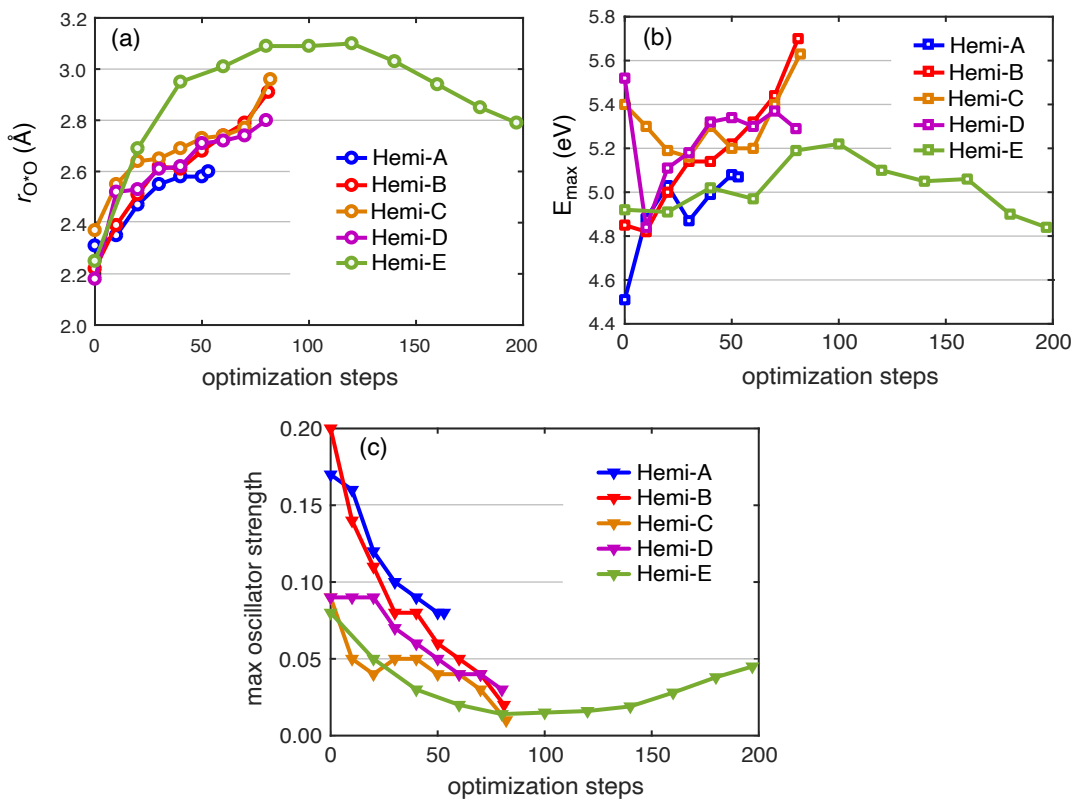
Figure S11: Evolution of (a) r_{O^*O}, (b) E_{max} (the excitation energy associated with the largest oscillator strength), and (c) largest oscillator strength, $\max_n\{f_{0,n}\}$, along MP2 geometry relaxations starting from hemibonded configurations of $^\bullet$OH(aq).
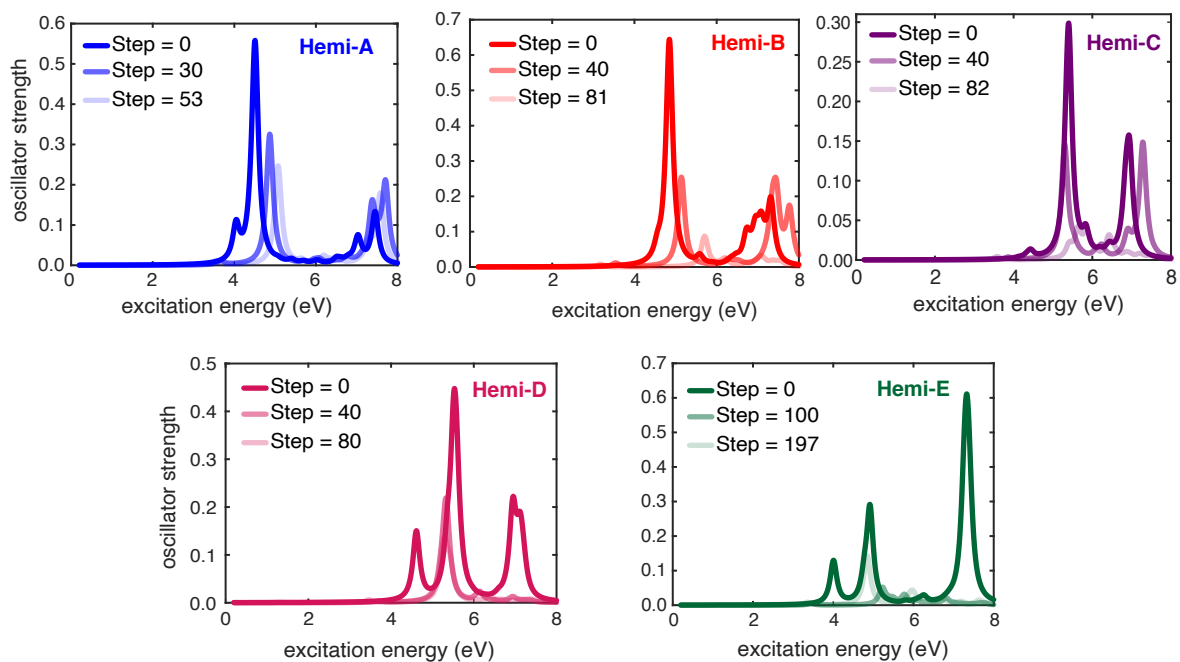
Figure S12: Evolution of TD-DFT spectra computed at the LRC-ωPBE/6-31++G* level (with $\omega = 0.398\ a_0^{-1}$) along MP2 geometry relaxation pathways initiated from hemibonded configurations of $^\bullet$OH(aq). A QM/MM approach is used wherein all water molecules within 5 Å of the hydroxyl moiety are included in the QM region, with point charges substituted for the rest. Although the spin charge gradually localizes onto the radical along the optimization path, as the $O^*\cdots O$ distance gradually increases (see Fig. S11), the most intense transition remains as a $1b_2(H_2O) \to 2p(^\bullet OH)$ charge-transfer excitation from a "pseudo-hemibonded" water molecule onto the radical. The intensity of this feature decreases with $O^*\cdots O$ distance but remains unmatched by any other spectral feature. The data for structure D are the same as those in Fig. 5b.
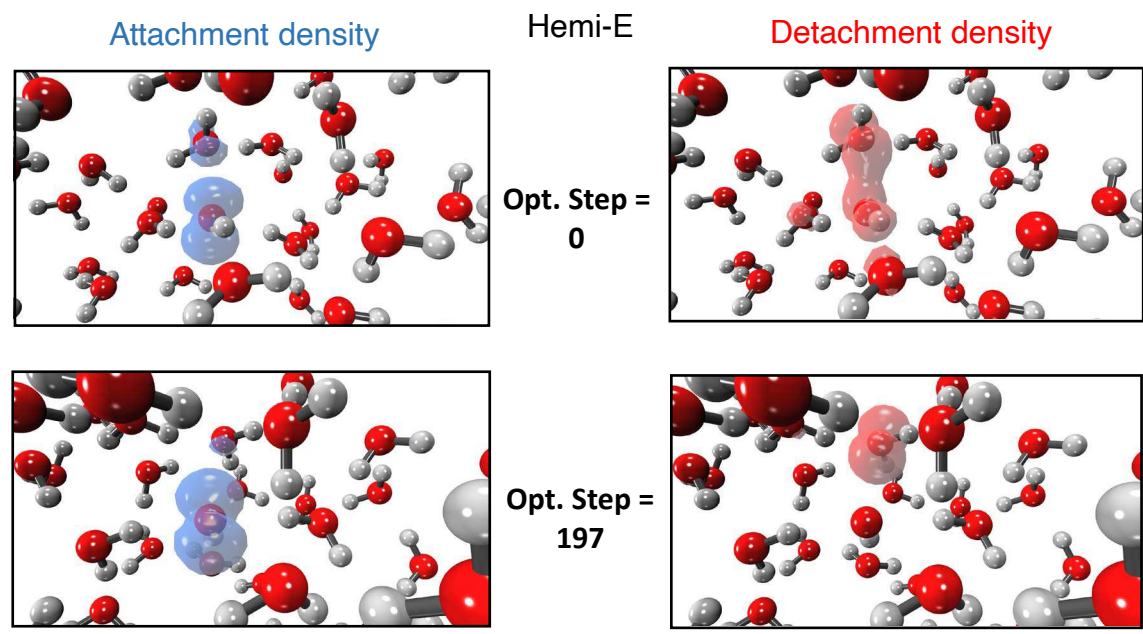
Figure S13: Attachment densities (blue contours) and detachment densities (red contours) associated with the most intense electronic transition, for the snapshot "Hemi-E" from Fig. S12, at both the starting and the ending point of a MP2 geometry relaxation that is initiated from a hemibonded configuration of $^\bullet$OH(aq). The nature of the transition remains the same (namely, charge transfer from H_2O to $^\bullet$OH) despite spin-localization and an increase in the $O^*\cdots O$ distance along the optimization trajectory.

Method	Exc. Energy	
	eV	nm
BH&HLYP	5.99	207
LRC-ωPBE[a]	5.16	240
OT-LRC-ωPBE[b]	5.42	229
Experiment[c]	5.40	230

[a] $\omega = 0.380\ a_0^{-1}$. [b] $\omega = 0.398\ a_0^{-1}$. [c] From Ref. 17.

Table S1: Excitation energies and wavelengths for absorption band maxima of $^\bullet$OH(aq). The spectra themselves are plotted in Fig. 3a (wavelength units) and Fig. S4 (energy units).

Functional	Hemibonded $\langle r_{O^*O} \rangle$ (Å)
B3LYP + D3	2.30
PBE0 + D3	2.34
LRC-ωPBE + D3	2.45

Table S2: Average $O^* \cdots O$ distance for hemibonded configurations of $^\bullet$OH(aq), as defined by $s_{OH} < 0.95$. The data are from QM/MM simulations reported in Ref. 9.

r_{O^*O} (Å)	Energy (Ha)	$\max_n\{f_{0,n}\}$	E_{max}[a] (eV)	s_{OH} (a.u.)
2.0	-152.042015	0.280	6.54	0.86
2.1	-152.047678	0.194	6.15	0.89
2.2	-152.051176	0.182	5.92	0.92
2.3	-152.053285	0.153	5.75	0.94
2.4	-152.054521	0.126	5.66	0.96
2.5	-152.055194	0.103	5.63	0.97
2.6	-152.055520	0.084	5.64	0.97
2.7	-152.055647	0.068	5.68	0.98
2.8	-152.055652	0.056	5.74	0.99
2.9	-152.055576	0.045	5.82	0.99
3.0	-152.055457	0.038	5.90	0.99
3.1	-152.055326	0.031	5.99	0.99
3.2	-152.055196	0.026	6.09	0.99
3.3	-152.055064	0.021	6.18	1.00
3.4	-152.054940	0.018	6.27	1.00
3.5	-152.054827	0.015	6.36	1.00

[a] Excitation energy corresponding to the largest oscillator strength.

Table S3: Properties of a hemibonded dimer, $^\bullet$OH(H$_2$O), as the $O^* \cdots O$ distance (r_{O^*O}) is varied, keeping the monomer geometries and orientation fixed. All the calculation were performed at the OT-LRC-ωPBE/ 6-31++G* level with $\omega = 0.412$ bohr^{-1}.

r_{O^*O} (Å)	Energy (Ha)	$\max_n\{f_{0,n}\}$	$E_{\max}{}^a$ (eV)	s_{OH} (a.u.)
2.0	-381.147074	0.236	5.89	0.80
2.1	-381.151131	0.239	5.43	0.83
2.2	-381.153151	0.217	5.04	0.86
2.3	-381.153934	0.188	4.73	0.89
2.4	-381.154036	0.157	4.49	0.91
2.5	-381.153788	0.129	4.31	0.93
2.6	-381.153381	0.104	4.19	0.95
2.7	-381.152929	0.084	4.12	0.96
2.8	-381.152483	0.067	4.10	0.97
2.9	-381.152060	0.054	4.10	0.97
3.0	-381.151675	0.044	4.12	0.97
3.1	-381.151337	0.035	4.17	0.97
3.2	-381.151038	0.029	4.23	0.98
3.3	-381.150762	0.023	4.30	0.98
3.4	-381.150513	0.020	4.37	0.99

[a]Excitation energy corresponding to the largest oscillator strength.

Table S4: Properties of a hemibonded pentamer, $^\bullet OH(H_2O)_4$, as the $O^* \cdots O$ distance (r_{O^*O}) is varied, keeping the monomer geometries and orientation fixed. All the calculation were performed at the OT-LRC-ωPBE/6-31++G* level with $\omega = 0.328$ bohr^{-1}.